

# Trajectories of a droplet driven by an internal active device

L. Rückert,<sup>1</sup> A. Zippelius,<sup>1</sup> and R. Kree<sup>1, a)</sup>

*Institut f. Theoretische Physik, Universität Göttingen, Friedrich-Hund Pl. 1, 37077 Göttingen, Germany*

(Dated: 3 May 2022)

We consider a liquid droplet which is propelled solely by internal flow. In a simple model, this flow is generated by an autonomous actuator, which moves on a prescribed trajectory inside the droplet. In a biological system, the device could represent a motor, carrying cargo and moving on a filamentary track. We work out the general framework to compute the self-propulsion of the droplet as a function of the actuating forces and the trajectory. The simplest autonomous device is composed of three point forces. Such a device gives rise to linear, circular or spiraling motion of the droplet, depending on whether the device is stationary or moving along a radial track. As an example of a more complex track we study in detail a spherical looped helix, inspired by recent studies on the propulsion of *Synechococcus*<sup>1</sup> and *Myxobacteria*<sup>2</sup>. The droplet trajectories are found to depend strongly on the orientation of the device and the direction of the forces relative to the track with the possibility of unbounded motion even for time independent forcing.

PACS numbers: 47. 63. Gd, 87. 17. Jj, 87. 85. Tu

## I. INTRODUCTION

Micro- and nanoscale medical robotics is a rapidly emerging area of research, which may open the way to many new and fascinating applications like precision surgery, directed drug delivery, micro-diagnostic sensing, uptake of toxins and many others (for recent reviews see<sup>3</sup> and<sup>4</sup>). A most important challenge on the way towards reliable bio-technological systems is to find bio-compatible, long lasting, and precisely controllable methods of propulsion *in vivo*. Magnetically actuated helical micro-motors on the  $10\mu\text{m}$  lengthscale, which are driven and controlled by external fields provide a promising example. They have been used for important manipulations of soft materials, in particular for steerable locomotion in small droplets, for the actuation of Human B lymphocytes and the assembly or disassembly of complexes of droplets and cells<sup>5</sup>. Furthermore they have already been actuated in the peritoneal cavity of a mouse<sup>6</sup> for deep tissue analysis. Another promising technique is the biohybrid actuation, which uses molecular motors of biological systems as propulsion mechanism. The big advantage of this approach is that fuel is provided by the surrounding biofluid, and these motors are highly optimised to convert the chemical energy into 3d propulsion<sup>7,8</sup>.

In many aspects of biohybrid systems can we profit from copying evolutionary optimized designs from natural biological systems. In the case of self-propulsion<sup>9</sup>, the design of artificial swimmers is inspired by biological microswimmers, such as algae, bacteria and eukaryotic cells. Many of these have special organelles, e.g. flagellae or cilia to propel the microorganism. However, swimming without specialised organelles is also found in

nature. Examples are *Myxobacteria*, gliding on a solid substrate, or *Synechococcus*, swimming in the ocean. In both cases one models the driving mechanism by motors running along helical tracks<sup>1,2</sup>.

In the present work, we want to explore possibilities of actuating a soft droplet by small internal motors, which operate autonomously. In<sup>10</sup>, the locomotion of a spherical squirmer encapsulated inside a droplet of comparable size suspended in another viscous fluid has been studied. In this work, it is shown that the engaged swimmer is able to propel the droplet, and in some situations both remain in a stable co-swimming state. In<sup>11</sup>, the co-swimming of a squirmer in a droplet with a nonuniform surface tension was studied. It was shown i.a. that the surface distribution can increase or decrease both velocities, that of the squirmer and that of the droplet.

Here, we consider rigid active swimmers of much smaller size, which are bound to follow a pre-defined trajectory. For biological motors, which typically operate on filaments of a network, this is a natural assumption. For field actuated motors, this has to be enforced by an external control mechanism. An enormous variety of droplet trajectories results, even for the simplest actuators, such as a Stokeslet or a rotlet, depending on the predefined trajectory of the actuator. As mentioned above, we focus here on a simple autonomous device, modelled by point forces, such that the device is force and torque free. Starting with simple settings, such as a stationary device, we compute the internal flow and the propulsion of the droplet in dependence on the position and orientation of the device. We then introduce devices which are moving with given speed on a prescribed filamentary track of increasing complexity. The simplest case is a device with uniform speed on a radial track, giving rise to spiralling motion. More complex trajectories are inspired by recent models of

<sup>a)</sup>Electronic mail: kree@theorie.physik.uni-goettingen.de



will be called momentary material frame (MMF). Once the flow field  $\mathbf{v}(\mathbf{r}, t)$  in the interior has been computed from Eq. (1) in the MMF, the linear and angular momentum of the droplet follow from

$$M\mathbf{v}_{CM} = \int_V d^3x \mathbf{v}, \quad I\boldsymbol{\omega} = \int_V d^3x \mathbf{r} \times \mathbf{v}. \quad (3)$$

The total mass is given by  $M = 4\pi/3$  and the moment of inertia by  $I = 8\pi/15$ . The subscripts in  $\mathbf{v}_{CM}$  refer to the center of mass and the integral is over the volume of the droplet,  $V$ . Here and in the following we use the notation  $\mathbf{v}(\mathbf{r})$  for the interior and  $\mathbf{v}^+(\mathbf{r})$  for the exterior flow field.

We consider  $\mathbf{R}(s)$  as part of a statistically homogeneous and isotropic network of thin and rigid filaments (see Fig.1)). If the network is dense, its effects on the internal flow are important and the system may be described as a permeating gel (see Ref.<sup>15</sup>). Here we consider the opposite limit of a sparse network, and neglect the effects of the filaments on the internal flow. The whole rigid network is freely floating in the interior of the droplet and will perform rigid body motion, characterised by  $\mathbf{v} = \mathbf{v}_{CM} + \boldsymbol{\omega} \times (\mathbf{r} - \mathbf{r}_{CM})$  with  $\mathbf{v}_{CM}$  and  $\boldsymbol{\omega}$  from Eq.(3), as explained in Ref.<sup>16</sup>. While the device is moving along the filament, its orientation, characterised by  $\mathbf{F}, \mathbf{d}$  may change. As the device is rigidly attached to the filamentary track, its orientation is assumed to be fixed with respect to the curve  $\mathbf{R}(s)$ , e.g. the forces are always tangential to  $\mathbf{R}(s)$ . The more general case will be discussed elsewhere<sup>17</sup>.

A trajectory of the droplet can be regarded as a sequence of snapshots. The actual computation of the droplet's trajectory is done by iteration. At time  $t$ , the device is at  $\mathbf{r}_0(t)$  and has orientation  $\mathbf{d}(t)$ . The Stokes equation is solved for this configuration in the MMF with momentary orientation  $\{\mathbf{e}_i\}$ , yielding the flow field  $\mathbf{v}(t)$ , which in turn determines  $\mathbf{v}_{CM}$  and  $\boldsymbol{\omega}$  according to Eq. 3. Next, the droplet is translated and rotated in the LF according to the droplet's equations of motion<sup>16</sup>

$$\mathbf{r}_{CM}(t + \Delta t) = \mathbf{r}_{CM}(t) + \sum_{i=1}^3 v_{CM,i}(t) \mathbf{e}_i(t) \Delta t \quad (4)$$

$$\mathbf{e}_i(t + \Delta t) = \mathbf{e}_i(t) + \boldsymbol{\omega}(t) \times \mathbf{e}_i(t) \Delta t. \quad (5)$$

The device is updated accordingly: it moves with speed  $U(t)$  to a new position  $\mathbf{r}_0(t + \Delta t)$  and its new orientation is determined by the new position on the prescribed space curve. Given the new position of the device and its orientation, the next iteration step can be performed.

Finally, we simplify the analysis by the additional assumption that the droplet's shape stays spherical. For finite interface tension  $\gamma_0$ , a flow field generated by the active device may deform the initial shape of the droplet. Such deformations become small, if  $\gamma_0$  is large compared to the deforming tractions generated by the flow field. In the following, we will always treat the spherical shape as persistent. Note that in this case, the droplet is not

propelled by shape changes, but exclusively by viscous forces emerging from the internal flow fields.

### III. ANALYTICAL SOLUTION

Due to the linearity of the Stokes equation, the flow field for any distribution  $\mathbf{f}$  of force densities can be calculated from the solution for a point force, i.e. from the Green's function  $\mathcal{G}(\mathbf{r}, \mathbf{r}_0)$ . In an unbounded fluid,  $\mathcal{G}(\mathbf{r}, \mathbf{r}_0)$  is the well-known Oseen tensor<sup>13</sup>, which for our purposes has to be modified due to the presence of the droplet and its interface. We have constructed  $\mathcal{G}(\mathbf{r}, \mathbf{r}_0)$  by standard methods (see appendix A), but as we do not need the full expression in the following we only sketch the main steps.

We use spherical coordinates and expand the point force density and the flow field in terms of vector spherical harmonics (VSH), whereby the boundary conditions become simple linear equations. Our choice of VSH is  $\mathbf{Y}_{lm}^{(0)} = \mathbf{e}_r Y_{lm}$ ,  $\mathbf{Y}_{lm}^{(1)} = r \nabla Y_{lm}$  and  $\mathbf{Y}_{lm}^{(2)} = \mathbf{e}_r \times \mathbf{Y}_{lm}^{(1)}$ . The expansion of the force density is explicitly given by

$$\mathbf{F}\delta(\mathbf{r} - \mathbf{r}_0) = \frac{\delta(r - r_0)}{r_0^2} \sum_{s=0}^2 \sum_{lm} f_{lms}(\Omega_0) \mathbf{Y}_{lm}^{(s)}(\Omega) \quad (6)$$

with  $f_{lms}(\Omega_0) = A_l^{(s)} [\mathbf{Y}_{lm}^{(s)}(\Omega_0)]^* \cdot \mathbf{F}$ . The prefactors  $A_l^{(s)} = (l(l+1))^{-1/2}$  for  $s = 1, 2$  and  $A_l^{(0)} = 1$  result from the normalisation of the VSH. The flow field which is generated by the above point force is similarly expanded in VSH

$$\mathbf{v}(\mathbf{r}, \mathbf{r}_0) = \sum_{s=0}^2 \sum_{lm} v_{lms}(r, \mathbf{r}_0) \mathbf{Y}_{lm}^{(s)}(\Omega). \quad (7)$$

The  $\{v_{lms}\}$  are constructed by a superposition of a special solution of the inhomogeneous equation and the general solution of the homogeneous equation in order to satisfy the boundary conditions.

This provides an exact analytic solution of the flow field of our model in terms of an infinite series. The applicability of this result may be limited by the rate of convergence of the series. For our purposes of calculating the droplet trajectories, however, it proves to be very convenient, because the total momentum and angular momentum of the droplet are determined exclusively from the  $l = 1$  component. Inserting the expansion of  $\mathbf{v}$  into Eq.3 reveals (see Ref.<sup>16</sup>):

$$\mathbf{v}_{CM} = \frac{1}{4\pi} \sum_m \int_{\partial V} d\Omega v_{1m0}(r = 1, \mathbf{r}_0) Y_{1m}(\Omega) \mathbf{e}_r \quad (8)$$

$$\boldsymbol{\omega} = -\frac{15}{8\pi} \sum_m \int_V d^3r r^2 v_{1m2}(r, \mathbf{r}_0) \nabla Y_{1m}(\Omega). \quad (9)$$

The details of the solution are given in the appendices; here we just give the complete solution for the rotational

velocity in order to illustrate the general type of flow field generated by a point force:

$$v_{1m2}(r, \mathbf{r}_0) = -\frac{f_{1m2}(\Omega_0)}{3\eta^-} \left( \frac{\eta^+ - \eta^-}{\eta^+} r r_0 + \Theta(r - r_0) \frac{r_0}{r^2} + \Theta(r_0 - r) \frac{r}{r_0^2} \right) \quad (10)$$

$$f_{1m2}(\Omega_0) = \mathbf{F} \cdot (\mathbf{r}_0 \times \nabla) Y_{1m}(\Omega_0) / \sqrt{2} \quad (11)$$

and a similar expression for  $v_{1m0}(r, \mathbf{r}_0)$  and  $v_{1m1}(r, \mathbf{r}_0)$  (see appendices).

#### IV. RESULTS

We are now able to calculate the droplet's motion generated by any device consisting of point forces and moving along an arbitrary trajectory. A systematic study of such motions generated by autonomous as well as externally actuated devices will be given elsewhere<sup>17</sup>. Here we restrict the discussion to the autonomous device Eq.(2), and first consider the simplest situation of a device fixed at one point in the CMF. In this case, features of the corresponding droplet trajectories can be understood qualitatively from symmetry arguments. Subsequently the results of a stationary device can be used to construct droplet trajectories moving along a straight radial filament. In general, the geometry of filamentary tracks within a microorganism or a droplet equipped with actin filaments, crosslinkers and active molecular motors<sup>18</sup> is much more complex. To study the propulsive forces, which are generated by the motion of autonomous devices along such tracks, we have chosen one illustrating case of filaments, which mimics the looped helix found in *Myxobacteria*<sup>2</sup>. Such a helical track also underlies the traveling cargo model of the swimming motility of *Synechococcus*<sup>1</sup>. However, we do not aim to contribute to a discussion of the propulsion of these microorganisms. Our intent is to study the motion of spherical droplets generated entirely by internal flow, which is due to active biohybrid devices. In particular, we do not consider surface deformations, which are a decisive part of the models discussed in<sup>1,2</sup>.

Furthermore, we consider only a single autonomous device moving along a prescribed track, which constitutes an elementary mechanism of propulsion. The flow of a collection of devices can be obtained by linear superposition of translational and rotational velocities in the CMF. A single device will typically exert only a very tiny force on the internal fluid. In dimensionless units, we use  $|\mathbf{d}| = 0.05$ ,  $|\mathbf{F}| = 1$ , viscosities  $\eta_- = 1$  and  $\eta_+ = 0.1$  and a droplet radius  $R = 1$  throughout this section. To compare to realistic systems, let us introduce units of length ( $\mu\text{m}$ ), time (seconds) and force ( $\text{pN} = 10^{-9}\text{N}$ ), and assume that the ambient fluid is water with  $\eta_+ = 0.89 \cdot 10^{-6} \text{pN}/(\text{sec} \cdot \mu\text{m}^2)$ . Then a dimensionless force of unit strength,  $|\mathbf{F}| = 1$ , corresponds to  $\approx 10^{-5} \text{pN}$ . Such a force on the fluid can, for example, be generated by a spherical particle of radius  $0.1\mu\text{m}$  moving

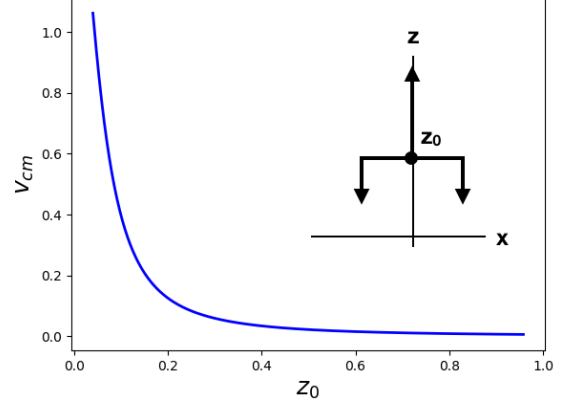


FIG. 2. Translational velocity of the droplet generated by a stationary device vs. distance of the device position from the droplet's center; the orientation of the device is such that  $\mathbf{F}$  is parallel to the  $z$ -axis (defined by  $\mathbf{r}_0$ ) and  $\mathbf{d}$  is parallel to the  $x$ -axis as indicated.

with velocity  $1\mu\text{m}/\text{sec}$ . These numbers are realistic for a molecular motor, moving at speed of order  $1\mu\text{m}/\text{sec}$  and transporting cargo of size about  $0.1\mu\text{m}$ . All the figures shown in this section will be given in these units, i.e. they correspond to a droplet of radius  $1\mu\text{m}$ , a device of length scale  $0.1\mu\text{m}$  and an internal fluid, which is 10 times as viscous as water.

Let us now consider a device fixed at  $\mathbf{r}_0$  in the CMF. By choice of coordinates we may put it on the  $z$ -axis of the CMF without loss of generality. In the simplest situation,  $\mathbf{F}$  is chosen as parallel to the unit vector  $\mathbf{e}_z$  of the  $z$  direction, so that  $\mathbf{d}$  is parallel to another cartesian axis that we chose as the  $x$ -axis. The setting is illustrated in the inset of Fig.(2). It is obvious by symmetry that the resulting trajectory of the droplet corresponds to uniform motion with velocity  $\mathbf{v}_{cm} = v_{cm}\mathbf{e}_z$ , which may depend upon the distance of the device from the droplet's center. The quantitative result is shown in Fig.(2), which reveals that the velocity is decreasing if the device is approaching the droplet's boundary. By symmetry, there is no internal chiral flow, which would cause a rotation of the CMF with respect to the LF. This can also be inferred from Eqs.(10, 11).

If  $\mathbf{F}$  is rotated around the  $y$ -axis,  $\mathbf{e}_z$  remains in the plane of the device spanned by  $\mathbf{F}$  and  $\mathbf{d}$ . In this case the droplet becomes a circular swimmer in the  $x$ - $z$  plane, because the CMF is rotated uniformly around the  $y$ -axis in the LF, which is plausible by symmetry and which again can be inferred from Eqs.(10, 11). Fig.(3) shows the angular velocity,  $\Omega$ , of a droplet on a circular trajectory, driven by a device with orientation  $\mathbf{F} \parallel -\mathbf{e}_x$  and  $\mathbf{d} \parallel \mathbf{e}_z$ . The angular velocity increases if the device approaches the boundary and larger magnitudes of the angular velocity lead to smaller radii of the circular trajectory. Thus a device moving along a radial filament from  $z_i$  to  $z_f > z_i$  will generate a planar, spiralling motion of the droplet as

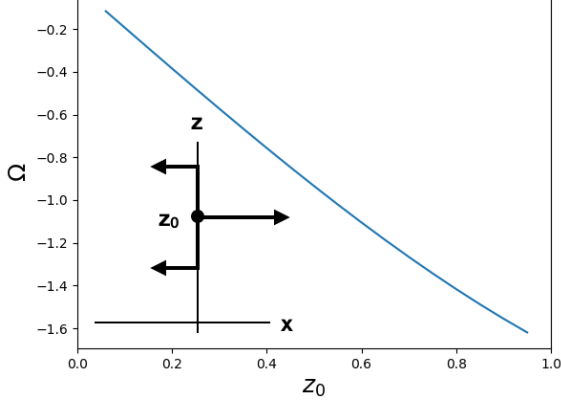


FIG. 3. Angular velocities of the droplet generated by a stationary device with  $\mathbf{F}$  oriented parallel to the x-axis and  $\mathbf{d}$  parallel to the z-axis (as indicated) vs. distance of the device position from the droplet's center.

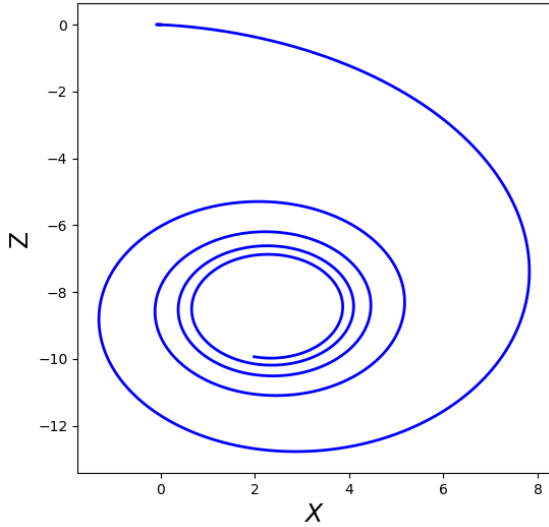


FIG. 4. Droplet trajectory generated by the device with  $\mathbf{F}$  oriented parallel to the x-axis and  $\mathbf{d}$  parallel to the z-axis, moving with constant velocity from  $z_i = 0.06$  to  $z_f = 0.94$ .

shown in Fig(4) for a device with constant velocity.

We conclude that a stationary autonomous device can propel the droplet; the trajectory of the droplet corresponds to linear or circular motion depending on the orientation of the device. Given that the magnitude of  $\mathbf{v}_{CM}$  depends on the distance of the device to the droplet center, the trajectory of a device moving with constant speed on a radial track is a spiral.

From the discussion of these simple cases it should be obvious that the relation between device motion and droplet motion is not straightforward. To illustrate the propulsive effects of devices moving along more complex

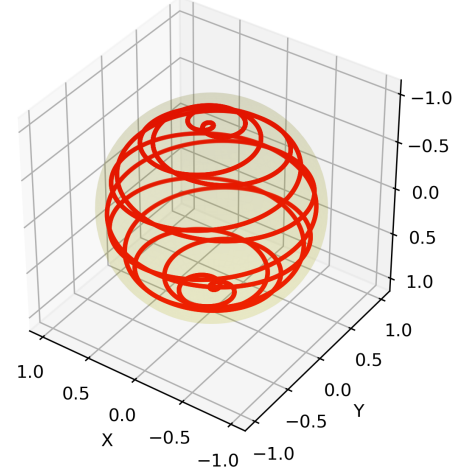


FIG. 5. The model filament of the “Synechococcus droplet” from Eq. (14) for  $k = 6$  and  $r_p = 0.9$ . The track starts at the north pole in x-direction.

filaments, we now consider the case of a “Synechococcus droplet”, i.e. a droplet with a simple autonomous device moving along a spherical looped helix. As a particular example, we choose the trajectory  $\mathbf{r}_0(t)$  in the CMF as

$$x_0(t) = r_p \sin t \cos(2kt) \quad (12)$$

$$y_0(t) = r_p \sin t \sin(2kt) \quad (13)$$

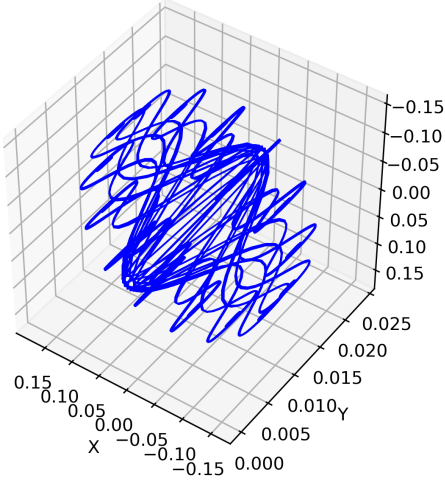
$$z_0(t) = r_p \cos t \quad (14)$$

with integer  $k$ . Fig(5) depicts this space curve for our choice  $k = 6$ .

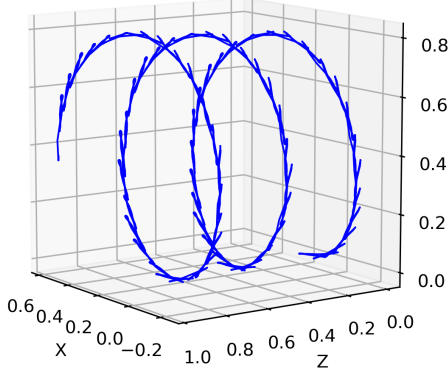
From all possible orientations of  $\mathbf{F}$  with respect to the spherical helix, we have selected 3 representative cases with  $\mathbf{F}$  parallel to one of the 3 directions (tangential, normal, binormal) of the Frénet Dreibein. For each of these orientations the device axis  $\mathbf{d}$  may be oriented along the remaining 2 directions of the Dreibein.

In the following, we will also allow for a special, explicit time dependence of the forcing, which is a decisive ingredient of the travelling cargo model of refs.<sup>1,2</sup>, where it is necessary to generate unbounded linear motion. In these models a high-drag cargo is transported in one direction along the helix, and at a pole is exchanged by low drag-cargo moving in the other direction. In our model, the magnitude of the force  $\mathbf{F}$  will switch between  $F$ , whenever it is heading southwards, and  $0.1F$ , when the device is heading northwards. We will compare the generated trajectories of this model to those generated by constant forcing and in particular address the question, whether it is possible to obtain unbounded linear motion also from constant forcing by appropriately oriented devices.

For the case of tangential force and normal axis, the trajectories are shown in Fig.(6). For constant force the



(a)



(b)

FIG. 6. Droplet trajectories for  $\mathbf{F}$  tangential and  $\mathbf{d}$  normal and for times up to  $t_{max} = 50\pi$  and. (a): time-independent force, (b): switching the forcing at the poles leads to an unbounded spiral trajectory.

periodic motion of the device along the looped helix results in a complex trajectory of the droplet, which is localised in a finite region in the LF. Switching the forcing at the poles turns the droplet into a spiral swimmer, with a substructure of the trajectory along the spirals due to the sudden change of  $\mathbf{F}$ .

The trajectories depend crucially on the orientation of the device axis  $\mathbf{d}$ , as is illustrated in Fig.(7), which still corresponds to purely tangential force, but now  $\mathbf{d}$  is oriented along the binormal. Comparing Figs. (6) and (7) one observes qualitatively different trajectories, even

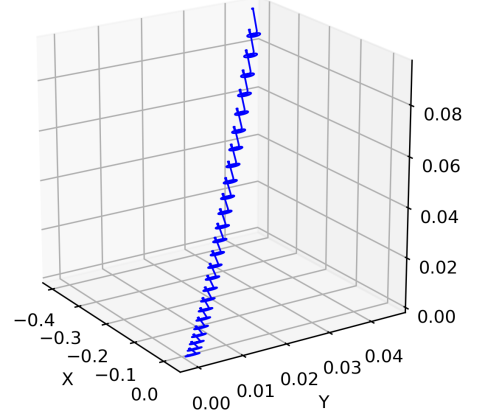


FIG. 7. Droplet trajectories for  $\mathbf{F}$  tangential and  $\mathbf{d}$  binormal and times up to  $t_{max} = 50\pi$ . The magnitude of the force is switched at the poles as described in the main text, resulting in an unbounded trajectory.

though only the orientation of  $\mathbf{d}$  has been changed. In both cases do the trajectories remain bounded in a finite domain for time independent force, whereas the switching of the force at the poles leads to unlimited displacements. But note that the distances traveled in z-direction differ by an order of magnitude.

Somewhat surprisingly, trajectories for  $\mathbf{F}$  in binormal direction do not stay bounded, even for time-independent  $\mathbf{F}$  as can be seen from Fig.(8). Qualitatively this can be understood from the fact that for a helix with many loops the binormal vector has a large component in z-direction for all points along the looped helix. Consequently, switching to smaller  $\mathbf{F}$  at the south pole, just decreases the droplet velocity in z-direction, as confirmed by data not shown.

As the figures show, the translational velocity of the droplet, which can be achieved by the motion of a single device along the helix is  $\approx 0.01\mu\text{m}/\text{sec}$ , which at first sight seems to be quite small. But it must be kept in mind that the motion is caused by a single micro-device with forces  $|\mathbf{F}| \sim 10^{-5}$  pN, moving at speeds of  $\sim \mu\text{m}/\text{sec}$ . To reach swimming speeds of  $\sim 10\mu\text{m}/\text{sec}$  a single device exerting forces of  $\sim 10^{-2}$  pN is necessary or, alternatively, the cooperative motion of several devices.

## V. CONCLUSIONS

We have calculated the trajectories of a spherical droplet, which is driven by an internal autonomous device moving along a filamentary track. The filament is



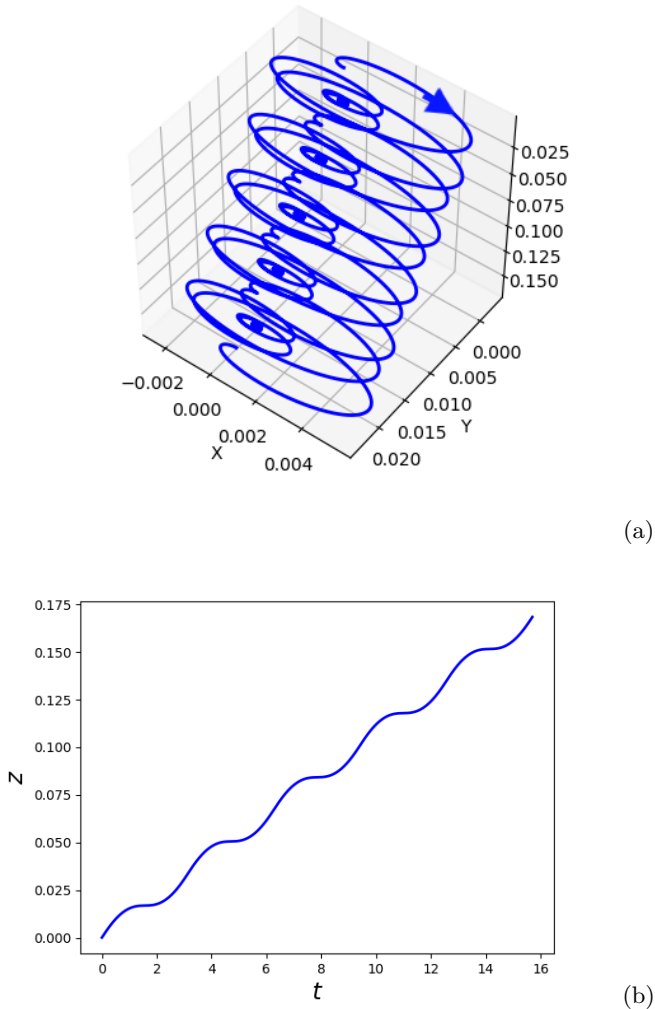


FIG. 8. Droplet trajectories up to  $t_{max} = 5\pi$  for  $\mathbf{F}$  binormal and  $\mathbf{d}$  tangential. (a): time-independent force, (b):  $z_{cm}(t)$  vs  $t$  for the trajectory shown in the panel above.

part of a sparse, isotropic and homogeneous rigid network, which is freely floating within the droplet. If the device can be described as a collection of closely neighbored point forces, the velocity of the droplet's center of mass and the angular velocity of the rigid network can be obtained analytically from Stokes equations. In general, a huge variety of droplet trajectories can be observed, depending on the orientation of the device and the track it is moving on.

The simplest case is a device, which is fixed within the network, and for which the  $\mathbf{F} - \mathbf{d}$  plane contains the  $z$ -axis, the resulting droplet motion is circular in general, with the exception of devices with  $\mathbf{F} \parallel \mathbf{e}_3$ , which lead to linear uniform motion. The angular velocity is increasing and the linear velocity is decreasing with the distance of the device from the droplet's boundary. These results allow to qualitatively understand the spiralling trajec-

tories, which are generated by a device moving along a radial track. If one is interested in unbounded linear propulsion of a droplet generated by an autonomous device of the type discussed here, the best choice would be to orient  $\mathbf{F}$  radially and in the direction of propulsion. Any small deviation of the orientation will, however, turn the droplet into a circle swimmer. To achieve stable linear propulsion, more complex trajectories of the device will be necessary. As one illustrative example of such trajectories we considered a looped spherical helix ("Synecococcus droplet"), inspired by the traveling cargo model of Ref.<sup>1,2</sup>. We showed that the droplet can be propelled by the internal flow generated by a device moving along this trajectory without any surface distortions. For time-independent forces, defined as tangential or normal to the looped helix, the droplet follows complex trajectories, which stay in a bounded region and which strongly depend upon the orientation of the device axis  $\mathbf{d}$ . If the forces exerted by the device on the fluid are switched between two values, whenever the device trajectory crosses the south- or north-pole of the looped spherical helix, as is assumed in the traveling cargo model, the droplet is propelled linearly without bounds. The propulsion velocity is slowed down by an order of magnitude if  $\mathbf{d}$  is changed from normal to binormal direction. For forces parallel to the binormal, the cargo-switching is not necessary to generate unbounded motion. The unbounded propulsion can be understood qualitatively because a binormal  $\mathbf{F}$  has a large  $z$ -component for all points along the helix.

The average propulsion velocity resulting from a device with  $\mathbf{F} \sim 10^{-5}$  pN is between  $1\mu\text{m}/\text{sec}$  for a fixed, radially oriented device and  $\sim 0.01\mu\text{m}/\text{sec}$  for a device moving along the looped spherical helix. The advantage of helical tracks is the built-in preferred axis, which stabilises the direction of linear propulsion against fluctuations of the device orientation. There are several ways to achieve higher propulsion velocities. First, one may increase the force  $\mathbf{F}$ , as all velocities scale linearly with this force. Instead of a single device with larger forces, one may as well use the cooperative effect of several devices. Another way to achieve higher propulsion speed is to change the geometry of the track. For example we found that a reduction of the radius  $r_p$  of the spherical helix from  $r_p = 0.9$  to  $r_p = 0.5$  increases the droplet's propulsion speed by a factor of 3. From our discussion of the fixed device it is plausible that trajectories close to a radial axis with orientations of  $\mathbf{F}$ , which stay approximately parallel to this axis will produce larger linear propulsion speed.

While we have only studied an autonomous device as an illustrative case, it is also straightforward to apply our framework to externally actuated devices, as, for example, helical magnetic swimmers. Work along these lines is in progress<sup>17</sup>.

## Appendix A: The Oseen tensor in vector spherical harmonics

We want to find the solution of the Stokes equation

$$\eta \nabla^2 \mathbf{v}(\mathbf{r} | \mathbf{r}_0) - \nabla p + \mathbf{f}(\mathbf{r} - \mathbf{r}_0) = 0 \quad (\text{A1})$$

$$\nabla \cdot \mathbf{v} = 0$$

inside and outside of a droplet with appropriate boundary conditions at  $R = 1$  and with a point force inhomogeneity,  $\mathbf{f} = \mathbf{F} \delta(\mathbf{r} - \mathbf{r}_0)$  at  $\mathbf{r}_0$ . The Green's tensor with cartesian components  $\mathcal{G}_{ij}$  is related to this solution via

$$v_i(\mathbf{r} | \mathbf{r}_0) = \sum_j \mathcal{G}_{i,j}(\mathbf{r} | \mathbf{r}_0) F_{0,j} \quad (\text{A2})$$

To simplify the notation we suppress the  $\mathbf{r}_0$  dependence and write  $\mathbf{v}(\mathbf{r})$ , unless stated otherwise.

Our general strategy is to construct a special solution of the inhomogeneous equation and then add a homogeneous solution to match the boundary conditions. As a special solution of the inhomogeneous problem we can choose the classical Oseen tensor solution of a point force in an unbounded fluid<sup>13</sup>. However, the usual representation of this solution is not easy to match to boundary conditions on the surface of a sphere. Instead of expanding the Oseen solution into vector spherical harmonics (VSH), we prefer to construct the solution from Stokes equation in terms of VSH directly.

The VSH form a complete orthogonal set on the surface of a unit sphere with respect to the scalar product

$$(\mathbf{h}, \mathbf{g}) = \int d\Omega \mathbf{h}^*(\Omega) \cdot \mathbf{g}(\Omega). \quad (\text{A3})$$

While the  $\mathbf{Y}_{lm}^{(0)}$  have norm 1, the  $s = 1, 2$  fields have a norm of  $(A_l^{(s)})^{-1} = \sqrt{\ell(\ell+1)}$ . For further properties of these functions we refer the reader to<sup>19</sup>.

According to our strategy, we start from the expansion of the flow fields and the point force in VSH, which are

given explicitly in Eqs.(6,7). In addition, the pressure is expanded in scalar spherical harmonics  $Y_{lm}$ :

$$p(\mathbf{r}) = \sum_{lm} p_{lm}(r) Y_{lm}(\Omega). \quad (\text{A4})$$

Before we embark on the the construction of the Oseen solution in terms of VSH let us briefly recall the solution of the homogeneous problem<sup>16</sup>, i.e. all  $f_{lms} = 0$ . Then, the Laplace equation for  $p$  is solved for  $r < 1$  by inner solutions  $p \propto r^\ell$ , which stay finite at  $r = 0$  and for  $r > 1$  by outer solutions  $p^+ \propto r^{-\ell-1}$  which vanish at infinity. Given the simple power laws for the pressure, the flows can easily be obtained as

$$v_{lm0}^+(r) = a_{lm}^+ r^{-\ell} + b_{lm}^+ r^{-\ell-2} \quad (\text{A5})$$

$$v_{lm1}^+(r) = \frac{2-\ell}{\ell(\ell+1)} a_{lm}^+ r^{-\ell} - \frac{1}{\ell+1} b_{lm}^+ r^{-\ell-2} \quad (\text{A6})$$

$$v_{lm2}^+(r) = c_{lm}^+ r^{-\ell-1}, \quad (\text{A7})$$

for outer solutions and

$$v_{lm0}(r) = a_{lm}^- r^{\ell+1} + b_{lm}^- r^{\ell-1} \quad (\text{A8})$$

$$v_{lm1}(r) = \frac{3+\ell}{\ell(\ell+1)} a_{lm}^- r^{\ell+1} + \frac{1}{\ell} b_{lm}^- r^{\ell-1} \quad (\text{A9})$$

$$v_{lm2}(r) = c_{lm}^- (r)^\ell \quad (\text{A10})$$

for inner solutions. We denote all quantities defined at  $r > 1$  by a +-superscript. The pressure modes are then given by  $p_{lm}^+(r) = \eta^+ \frac{4\ell-2}{\ell+1} a_{lm}^+ r^{-\ell-1}$  in the ambient fluid and by  $p_{lm}(r) = \eta^- \frac{4\ell+6}{\ell} a_{lm}^- r^\ell$  in the interior of the droplet.

Now we turn to the construction of a special solution of the inhomogeneous Eq.(A1) in the *interior* of the droplet. The functional forms of inner and and outer solutions of the homogeneous problem will turn out to be very convenient to construct an Ansatz for this inhomogeneous solution. First, we insert the expansions Eqs.(6, 7, A4) into, the Stokes equation Eq.(A1) and convert it into a system of ordinary differential equations for the  $v_{lms}$  and  $p_{lm}$  modes

$$\eta^- \begin{pmatrix} \left( \frac{d^2}{dr^2} + \frac{2}{r} \frac{d}{dr} \right) - \frac{(2+l(l+1))}{r^2} & \frac{2l(l+1)}{r^2} & 0 \\ \frac{2}{r^2} & \left( \frac{d^2}{dr^2} + \frac{2}{r} \frac{d}{dr} \right) - \frac{l(l+1)}{r^2} & 0 \\ 0 & 0 & \left( \frac{d^2}{dr^2} + \frac{2}{r} \frac{d}{dr} \right) - \frac{l(l+1)}{r^2} \end{pmatrix} \begin{pmatrix} v_{lm0} \\ v_{lm1} \\ v_{lm2} \end{pmatrix} = \begin{pmatrix} \frac{dp_{lm}}{dr} \\ \frac{p_{lm}}{r} \\ 0 \end{pmatrix} - \frac{\delta(r-r_0)}{r_0^2} \begin{pmatrix} f_{lm0} \\ f_{lm1} \\ f_{lm2} \end{pmatrix} \quad (\text{A11})$$

The pressure has to be determined from  $\nabla^2 p = \nabla \cdot \mathbf{f}$ , which results from the incompressibility. In terms of  $p_{lm}$

modes it takes on the form

$$\frac{d^2 p_{lm}}{dr^2} + \frac{2}{r} \frac{dp_{lm}}{dr} - \frac{l(l+1)}{r^2} p_{lm} = \frac{f_{lm0}}{r_0^2} \frac{d}{dr} \delta(r-r_0) + \frac{2f_{lm0}}{r_0^3} \delta(r-r_0) - \frac{l(l+1)f_{lm1}}{r_0^3} \delta(r-r_0). \quad (\text{A12})$$



Note that in Eq.(A11) the  $s = 0$  and the  $s = 1$  modes are still coupled, but we can use the incompressibility condition  $\nabla \cdot \mathbf{v} = 0$ , which becomes

$$\frac{dv_{lm0}}{dr} + \frac{2}{r}v_{lm0} - \frac{l(l+1)}{r}v_{lm1} = 0, \quad (\text{A13})$$

to express the  $v_{lm1}$  via the  $v_{lm0}$  and get two decoupled equations for each  $l, m$ ,

$$\begin{aligned} \eta^- \left( \frac{d^2 v_{lm0}}{dr^2} + \frac{4}{r} \frac{dv_{lm0}}{dr} + \frac{2-l(l+1)}{r^2} v_{lm0} \right) \\ = \frac{dp_{lm}}{dr} - \frac{f_{lm0}}{r_0^2} \delta(r-r_0) \end{aligned} \quad (\text{A14})$$

$$\eta^- \left( \frac{d^2 v_{lm2}}{dr^2} + \frac{2}{r} \frac{dv_{lm2}}{dr} - \frac{l(l+1)}{r^2} v_{lm2} \right) = -\frac{f_{lm2}}{r_0^2} \delta(r-r_0). \quad (\text{A15})$$

To obtain a special solution of the inhomogeneous equation, we will make use of these functional forms of outer and inner solutions for the regions  $r > r_0$  and  $r < r_0$ , respectively. First we solve Eq.(A12) for the pressure  $p$ . We construct the solution by matching the inner and outer homogeneous solution of this equation and thus use the ansatz:

$$p_{lm}(r) = A_{lm} r^\ell \Theta(r_0 - r) + B_{lm} r^{-\ell-1} \Theta(r - r_0). \quad (\text{A16})$$

Plugging this ansatz into Eq.(A12) determines the values of  $A_{lm}$  and  $B_{lm}$ ,

$$A_{lm} = \frac{-(\ell+1)f_{lm0} + \ell(\ell+1)f_{lm1}}{2\ell+1} r_0^{-\ell-2} \quad (\text{A17})$$

$$B_{lm} = \frac{\ell f_{lm0} + \ell(\ell+1)f_{lm1}}{2\ell+1} r_0^{\ell-1}. \quad (\text{A18})$$

Now the equation for  $v_{lm0}$  becomes

$$\begin{aligned} \eta^- \left( \frac{d^2 v_{lm0}}{dr^2} + \frac{4}{r} \frac{dv_{lm0}}{dr} + \frac{2-l(l+1)}{r^2} v_{lm0} \right) \\ = \ell A_{lm} r^{\ell-1} \Theta(r_0 - r) - (\ell+1) B_{lm} r^{-\ell-2} \Theta(r - r_0) \end{aligned}$$

Again, one can construct the solution by adding inner ( $r < r_0$ ) and outer ( $r > r_0$ ) parts. Special solutions of the inhomogeneous equation are easily identified as  $C_{lm} r^{\ell+1} \Theta(r_0 - r)$  for the inner and  $D_{lm} r^{-\ell} \Theta(r - r_0)$  for the outer part, respectively. To ensure the conditions  $v_{lm0}(r \nearrow r_0) = v_{lm0}(r \searrow r_0)$   $v'_{lm0}(r \nearrow r_0) = v'_{lm0}(r \searrow r_0)$  (here the prime denotes derivative with respect to  $r$ ), we have to add solutions of the homogeneous equation and thus end up with an ansatz of the form

$$\begin{aligned} v_{lm0}(r) = C_{lm} r^{\ell+1} \Theta(r_0 - r) + D_{lm} r^{-\ell} \Theta(r - r_0) \\ + F_{lm} r^{\ell-1} \Theta(r_0 - r) + G_{lm} r^{-\ell-2} \Theta(r - r_0) \end{aligned} \quad (\text{A19})$$

Note that for  $r > r_0$  we added a homogeneous solution which decays as  $r \rightarrow \infty$  to ensure the boundary condition

selecting the Oseen solution. Straightforward calculation gives the following result:

$$\begin{aligned} C_{lm} &= \frac{\ell}{4\ell+6} \frac{A_{lm}}{\eta^-} \\ D_{lm} &= \frac{\ell+1}{4\ell-2} \frac{B_{lm}}{\eta^-} \\ F_{lm} &= \frac{2D_{lm}}{2\ell+1} r_0^{-2\ell+1} - \frac{2\ell+3}{2\ell+1} C_{lm} r_0^2 \\ G_{lm} &= -\frac{2\ell-1}{2\ell+1} D_{lm} r_0^2 - \frac{2}{2\ell+1} C_{lm} r_0^{2\ell+3}. \end{aligned}$$

The constraint of incompressibility determines  $v_{lm1}$  from Eq.(A13). Finally, by matching inner and outer solutions we obtain  $v_{lm2}$  from Eq.(A15),

$$v_{lm2}(r) = -\frac{f_{lm2}}{\eta^-(2\ell+1)} \left( \Theta(r-r_0) \frac{r_0^\ell}{r^{\ell+1}} + \Theta(r_0-r) \frac{r^\ell}{r_0^{\ell+1}} \right). \quad (\text{A20})$$

The flow field, which was obtained as a special solution of the inhomogeneous equation, can be used to deduce the Oseen tensor expanded in vector spherical harmonics:

$$\mathcal{G}_{ij}^{(Oseen)}(\mathbf{r}, \mathbf{r}_0) = \sum_{s,s'} \sum_{lm} G_{lm}^{s,s'}(r, r_0) (\mathbf{Y}_{lm}^{(s)}(\Omega))_i (\mathbf{Y}_{lm}^{(s)}(\Omega_0))_j.$$

Inserting this expansion into Eq.(A2) yields

$$v_{lms}(r, \mathbf{r}_0) = \sum_{s'} G_{lm}^{s,s'}(r, r_0) f_{lms'}(\Omega_0) \frac{1}{A_l^{(s')}},$$

where we have made the dependence on  $\mathbf{r}_0$  explicit again. The chiral component can be read off directly from Eq.(A20)

$$\begin{aligned} \sqrt{\ell(\ell+1)} G_{lm}^{2,2}(r, r_0) = \\ -\frac{1}{\eta^-(2\ell+1)} \left( \Theta(r-r_0) \frac{r_0^\ell}{r^{\ell+1}} + \Theta(r_0-r) \frac{r^\ell}{r_0^{\ell+1}} \right). \end{aligned}$$

The other components require the inversion of a  $2 \times 2$  matrix, which is not needed here.

Having constructed a special solution to the inhomogeneous equation, one can now simply add the homogeneous flow fields to obtain the general solution and match the boundary conditions, which is explained in the next section.

## Appendix B: Matching boundary conditions

The flow at the outside is given by the homogeneous solution  $v_{lms}^+$ , while the flow on the inside is given by the superposition of the inhomogeneous and the homogeneous flow. The boundary conditions determine the six, yet unknown coefficients  $a_{lm}^\pm$ ,  $b_{lm}^\pm$  and  $c_{lm}^\pm$  of the homogeneous flow. There are 3 linear equations emerging

from the continuity of the flow velocity at  $r = 1$ , and another set of 3 linear equations emerging from the continuity of tractions:  $\mathbf{e}_r \cdot (\boldsymbol{\sigma}_+ - \boldsymbol{\sigma}_-) = 2\gamma_0 \mathbf{e}_r$ . As the  $s = 2$  mode only involves the  $c_{lm}^\pm$ , the  $6 \times 6$  matrix of coefficients splits into a  $2 \times 2$  block (coupling  $c_{lm}^\pm$ )  $\hat{\mathbf{M}}_2$  and a  $4 \times 4$  block  $\hat{\mathbf{M}}_0$ . The inhomogeneities in these linear equations are due to the special inhomogeneous solution inside. To determine all the terms in the linear equations we have to calculate the normal stress inside and outside of the droplet. For details of the calculation see<sup>16</sup>.

With  $\mathbf{Z}_0 = (a^+, b^+, a^-, b^-)^t$  and  $\mathbf{Z}_2 = (c^+, c^-)^t$  the boundary conditions become  $\hat{\mathbf{M}}_0 \mathbf{Z}_0 = \mathbf{I}_0$  and  $\hat{\mathbf{M}}_2 \mathbf{Z}_2 = \mathbf{I}_2$  with

$$\hat{\mathbf{M}}_0 = \begin{pmatrix} 1 & 1 & -1 & -1 \\ \frac{2-l}{l(l+1)} & \frac{-1}{l+1} & -\frac{l+3}{l(l+1)} & -\frac{1}{l} \\ 2\eta^+ \frac{l^2+3l-1}{l+1} & 2\eta^+(l+2) & \frac{2}{l}\eta^-(l^2-l-3) & 2\eta^-(l-1) \\ 2\eta^+(l^2-1) & 2\eta^+l(l+2) & -2\eta^-l(l+2) & -2\eta^-(l^2-1) \end{pmatrix}$$

and

$$\mathbf{I}_0 = \begin{pmatrix} D_{lm} + G_{lm} \\ \frac{2-l}{l(l+1)} D_{lm} - G_{lm}/(l+1) \\ B_{lm} + 2\eta^- l D_{lm} + 2\eta^-(l+2) G_{lm} \\ 2\eta^-(l^2-1) D_{lm} + 2\eta^- l(l+2) G_{lm} \end{pmatrix} \quad (\text{B1})$$

as well as

$$\hat{\mathbf{M}}_2 = \begin{pmatrix} 1 & -1 \\ \eta^+(l+2) & \eta^-(l-1) \end{pmatrix} \quad (\text{B2})$$

and

$$\mathbf{I}_2 = -\frac{\gamma_{lm} r_0^l}{\eta^-(2l+1)} \begin{pmatrix} 1 \\ \eta^-(l+2) \end{pmatrix} \quad (\text{B3})$$

The solutions for the  $c_{lm}^\pm$  can be obtained easily by

hand

$$c_{lm}^- = \frac{\frac{\ell+2}{2\ell+2} f_{lm2} \left( \frac{\eta^+}{\eta^-} - \frac{1}{2} \right) \frac{r_0^\ell}{a^{\ell+1}}}{\eta^-(\ell-1) + \eta^+(\ell+2)} \quad (\text{B4})$$

$$c_{lm}^+ = \frac{\frac{\ell+2}{2\ell+2} f_{lm2} \left( \frac{\eta^+}{\eta^-} - \frac{1}{2} \right) \frac{r_0^\ell}{a^{\ell+1}}}{\eta^-(\ell-1) + \eta^+(\ell+2)} - \frac{f_{lm2}}{\eta^-(2\ell+1)} \frac{r_0^\ell}{a^{\ell+1}}, \quad (\text{B5})$$

whereas the  $a_{lm}^\pm, b_{lm}^\pm$  obtained  $\hat{\mathbf{M}}_0^{-1} \mathbf{I}$  are complicated expressions, which are best manipulated by symbolic machine computation or numerical evaluation.

- <sup>1</sup>K. Ehlers and G. Oster, PLoS ONE **7**, e36081 (2012).
- <sup>2</sup>B. Nan, J. Chen, J. Neu, R. M. Berry, G. Oster, and D. R. Zusman, PNAS **108**, 2498 (2011).
- <sup>3</sup>J. Li, E.-F. de Avila, W. Gao, L. Zhang, and J. Wang, Science Robotics **2**, eaam6431 (2017).
- <sup>4</sup>C. Hu, S. Pane, and B. J. Nelson, Annu. Rev. Control Robot. Auton. Syst. **1**, 53 (2018).
- <sup>5</sup>Y. Ding, F. Qiu, X. C. i Solvas, F. W. Y. Chiu, B. J. Nelson, and A. deMello, Micromachines **7**, 25 (2016).
- <sup>6</sup>A. Servant, F. Qiu, M. Mazza, K. Kostarelos, and B. J. Nelson, Adv. Mat. **27** (2015).
- <sup>7</sup>A. F. and, Annu. Rev. Biomed. Eng. **17**, 243 (2015).
- <sup>8</sup>M. Kojima, Z. Zhang, M. Nakajima, K. Ooe, and T. Fukuda, Sens. Actuators B **183**, 395 (2013).
- <sup>9</sup>C. Bechinger, R. D. Leonardo, H. Löwen, C. Reichhardt, G. Volpe, and G. Volpe, Rev. Mod. Phys. **88**, 045006 (2016).
- <sup>10</sup>S. Y. Reigh, L. Zhu, F. Gallaire, and E. Lauga, Soft Matter **13**, 3161 (2017).
- <sup>11</sup>V. A. Shaik, V. Vasani, and A. Ardekani, J. Fluid Mech. **851**, 187 (2018).
- <sup>12</sup>C. Pozrikidis, *Boundary integral and singularity methods for linearized viscous flow* (Cambridge University Press, 1992).
- <sup>13</sup>S. Kim and S. J. Karrila, *Microhydrodynamics: Principles and Selected Applications* (Dover Publications, 2005).
- <sup>14</sup>A. Zöttl and H. Stark, J. Phys.: Condens. Matter **28**, 253001 (28pp) (2016).
- <sup>15</sup>R. Kree and A. Zippelius, Euro. Phys. J. E **41**, 118 (2018).
- <sup>16</sup>R. Kree, P. Burada, and A. Zippelius, J. Fluid Mech. **821**, 595 (2017).
- <sup>17</sup>L. Rückert, A. Zippelius, and R. Kree, (2019).
- <sup>18</sup>M. Weiss, J. Frohnmayer, L. Benk, B. Haller, J. J. T. Heitkamp, M. Börsch, R. Lira, R. Dimova, R. Lipowsky, E. Bodenschatz, J. Baret, T. Vidakovic-Koch, K. Sundmacher, I. Platzman, and J. Spatz, Nature Mat. **17**, 89 (2017).
- <sup>19</sup>B. Carrascal, G. Estevez, P. Lee, and V. Lorenzo, Eur. J. Phys. **12**, 184 (1991).